ACS OMEGA

http://pubs.acs.org/journal/acsodf

Article

A Low-Cost SiO_x/C@Graphite Composite Derived from Oat Husk as an Advanced Anode for High-Performance Lithium-Ion Batteries

Mengfei Sun, Jiaojiao Ma, Minghang Xu, Hongxun Yang,* Jianzi Zhang, and Changhua Wang

Cite This: *ACS Omega* 2022, 7, 15123−15131

Read Online

ACCESS | Metrics & More | Article Recommendations | Supporting Information

ABSTRACT: Silicon monoxide (SiO_x), as a promising anode for the next-generation high-power lithium-ion batteries, has some advantages such as higher lithium storage capacity (~2400 mAh g^{-1}), suitable working potential, and smaller volume variations during cycling compared with pure silicon. However, its disadvantages such as its inherent low conductivity and high cost impede its extensive applications. Herein, we have developed a low-cost and high-capacity SiO_x/C@graphite (SCG) composite derived from oat husks by a simple argon/hydrogen reduction method. For further practical application, we also investigated the electrochemical performances of SiO_x mixed with different ratios of graphite. As an advanced anode for lithium-ion batteries, the SCG-1 composite exhibits an excellent electrochemical performance in terms of lithium storage capacity (809.5 mAh g^{-1} at 0.5 A g^{-1} even after the 250th cycle) and high rate capability (479.7 mAh g^{-1} at 1 A g^{-1} after the 200th cycle). This work may pave the way for developing a low-cost silicon-based anode derived from biomass with a large reversible capacity and long cycle life in lithium-ion batteries.

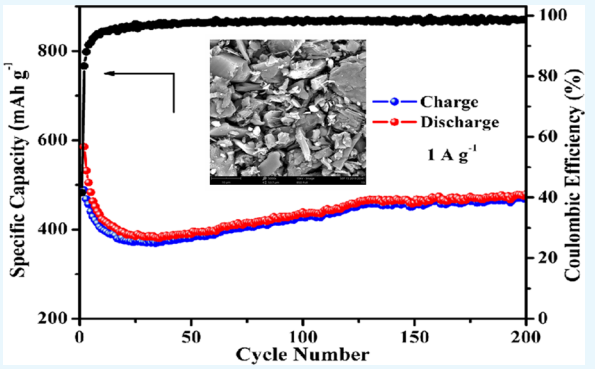

1. INTRODUCTION

As one of the most promising energy storage devices, lithium-ion batteries (LIBs) have been widely used in various fields in our modern lives.[1−3] However, with the rapid development of economy and society, various portable devices, new energy vehicles, and large-scale energy storage equipment have higher demands for the capacity, endurance, and service life of LIBs.[4,5] The commercial development of LIBs has reached a bottleneck stage. The negative electrode material is an important part of LIBs, which largely affects the electrochemical performance and safety of LIBs.[6] As far as the anode is concerned, the anode materials widely used by LIB manufacturers currently on the market are graphite-based carbon materials with a theoretical capacity of only 372 mAh g^{-1}.[7−9] In practical applications, they are close to the theoretical capacity. It is difficult to achieve higher capacity requirements, which is not enough to meet the energy density requirements of power LIBs. Therefore, the development of high-performance LIB anode materials is imperative. The anode materials based on alloying/dealloying and conversion reactions, such as Si (4200 mAh g^{-1}), P (2596 mAh g^{-1}), Sn (960 mAh g^{-1}), Sb (660 mAh g^{-1}), Ge (1600 mAh g^{-1}), and transition metal oxides, are considered as promising alternative high-capacity candidate materials.[10−12] In addition, polyanionic electrode materials such as phosphates, silicates, and borates have also been reported.[13] However, it is very challenging for those materials to be commercialized on a large scale for LIBs.

Among the emerging anode materials proposed for LIBs, silicon-based materials have some advantages of high theoretical specific capacity, low voltage platforms, and abundant content in the earth's crust,[14−19] exhibiting one of the most candidate materials to replace graphite. However, silicon-based anode materials also have obvious shortcomings.[20−25] In the process of repeated charging/discharging, the huge volume variations of silicon-based materials (about 300%) leads to the crushing and shedding of electrode materials and the overall performance of the battery is greatly reduced.[26−33] In addition, the inherent semiconductor characteristics of silicon is also another problem that cannot be ignored. For this reason, solving these defects of silicon materials is the current research topic at home and abroad, and silicon−carbon composites are the current major research hotspots.[34−39] The carbon materials show the obvious advantages of high electrical conductivity and relatively stable structure, a small volume expansion during the cycle (usually below 10%), and good flexibility and lubricity, which can inhibit the silicon material to a certain extent.[31,35] During the

Received: February 19, 2022
Accepted: April 12, 2022
Published: April 25, 2022

charging/discharging cycles, the silicon−carbon composite could combine the respective advantages of the silicon and carbon materials to show excellent performance.[32,36] Yan and Guo reduced the silica particles into porous Si by magnesium and then carried out carbon coating by chemical vapor deposition to obtain a silicon−carbon composite with an excellent specific capacity of 1835 mAh g^{-1} and cycle stability.[32] Recent studies have also shown that carbon-coated silicon oxide (C/SiO_x) composites when tested as anode materials for LIBs show superior performance compared with silicon-based anode materials.[40] The inert Li_4SiO_4 and Li_2O generated during the initial lithiation process could effectively prevent the agglomeration of nanosilicon particles and the expansion of the buffer volume during charge and discharge, thereby improving the cycle stability and rate performance of the electrode to a certain extent. In addition, carbon coating could also better buffer volume expansion, improve electrical conductivity, and hinder the aggregation of SiO_x particles.[41]

On the other hand, biomass materials have also been extensively studied due to their renewable, abundant resources, and low cost as energy storage and conversion devices.[42] Zhao et al. prepared hierarchical N, P codoped porous 3D-carbon framework@TiO_2 nanoparticle hybrid by using pollen as a biomass precursor through a facile template-assisted sol−gel method, which exhibits excellent electrochemical performance when used in LIBs.[43] Some biomasses such as rice husks, oat husks, bamboo shoot hulls, and so forth are considered to be ideal sources of silicon due to the presence of silica.[44] Chen et al. prepared a hierarchically porous SiO_x/C and carbon materials from bamboo shoot hulls, showing a high capacity of 1289 mAh g^{-1} after 400 cycles at 200 mA g^{-1} as the anode for LIBs.[45] Therefore, the rational utilization of waste biomass materials can not only prepare electrode materials with excellent performance but also reduce the production cost of batteries. Oat husks are one of the most common biomass materials in the past few decades.[46] A large amount of oat husk waste is produced every year, most of which is incinerated or left in landfills. In fact, oat husks have a large amount of biosilica with amorphous properties of hydrated SiO_2 grains.[46] In the production of porous carbon materials and silicon, it is very meaningful to use oat husks in the near future. When oat husks are carbonized in the hydrogen/argon mixture, carbon-coated SiO_x materials can be directly obtained. As a buffer and conductive matrix, biochar can effectively alleviate the huge volume variations. Recently, we have reported a SiO_x/C@graphite composite derived from rice husk, which was studied at different temperatures.[47] To the best of our knowledge, there is no report about using oat husks mixed with different graphite ratios as negative electrode materials for LIBs.

Herein, we will develop a low-cost and high-capacity SiO_x/C@graphite (SCG) hybrid derived from oat husks via a simple argon/hydrogen reduction method. SiO_x nanoparticles act as active synergies for lithium storage active materials. The in situ carbon matrix networks derived from biomass act as an effective three-dimensional conductive network and spacer to improve rate capacity and buffer volume changes. Graphite can be used as a conductor to further improve the rate capability and cycle stability of SCG as negative electrodes of LIBs. At the same time, the influence of graphite content on the electrochemical performances of SCG composites was also explored.

2. EXPERIMENTAL SECTION

2.1. Preparation of SiO_x/C@Graphite Composite Material. In a typical procedure, the oat husks (5 g) were soaked in 2 M HCl solution (200 mL) at 60 °C for 8 h. The product was washed with deionized water to neutrality and then dried overnight at 60 °C in a blast drying oven. Then, the oat husks were placed in a tube furnace and heated to 450 °C in a nitrogen atmosphere for 2 h at a rate of 2 °C min^{-1} to obtain a precursor.

The obtained precursor (1 g) and graphite were uniformly mixed at a mass ratio of 1:1 and ball-milled for 5 h. Then, the collected ball mill product (2 g) was placed into a tube furnace and heated to 1100 °C at a heating rate of 3 °C min^{-1} in an argon/hydrogen (Ar/H_2) gas and maintained for 3 h and was naturally cooled to room temperature. The as-obtained product was a SiO_x/C@graphite composite (represented as SCG-1, and 1 represents a 1:1 ratio of precursor to graphite). For comparison, we adjusted the ratio of precursor to graphite according to the mass ratio of 1:0.5 and 1:2, which were recorded as SCG-0.5 and SCG-2, respectively.

2.2. Materials Characterization. The as-synthesized products were characterized by X-ray diffraction (XRD, Shimadzu XRD-6000, Cu Kα radiation), field emission scanning electron microscopy (SEM, JEOL, JSM6700F), energy-dispersive X-ray spectrometry, and transmission electron microscopy (FEI TF20 and JEM-2100F) from Shiyanjia Lab. The surface composition of the products was evaluated using XPS (Thermo ESCALAB 250XI). Thermogravimetric analysis was performed on a Pyris Diamond TG-DTA instrument under a nitrogen atmosphere. Raman analysis was performed on a Renishaw Raman spectrometer. The specific surface area and pore volume were estimated by nitrogen adsorption/desorption measurements at 77 K using a Micromeritics ASAP 2460 via the Brunauer−Emmett−Teller (BET) and Barrett−Joyner−Halenda (BJH) methods, respectively.

2.3. Electrochemical Measurements. The electrochemical performances of the as-obtained active materials were measured using the assembled 2032 coin-type half-cell. The working electrodes composed of 80 wt % of active materials, 10 wt % of conductive additives, and 10 wt % of poly(vinylidenedifluoride) as the binder. *N*-Methyl-2-pyrrolidone was used as the solvent. The mixed slurry was cast onto a piece of copper foil, dried in a vacuum oven at 60 °C for 12 h, and then cut into discs with a diameter of 13 mm. The loading mass of the as-prepared active materials on the electrode is about 1.26 mg cm^{-2}. Lithium foil was used as the reference electrode. $LiPF_6$ (1 M) in ethylene carbonate and diethylcarbonate (EC/DEC, 1:1 by volume) was used as the electrolyte. The galvanostatic charge−discharge tests were performed using a LAND CT-2001A (Wuhan, China) testing system at different current densities in the voltage range between 0.01 and 3.0 vs $(Li/Li^+)/V$. Cyclic voltammetry (CV) measurements were carried out on a CHI 760E (Chenhua Ltd. Co., China) electrochemical workstation between 0.01 and 3.0 vs $(Li/Li^+)/V$ at a sweep rate of 0.1 mV s^{-1}. Electrochemical impedance spectroscopy (EIS) tests were carried out on an electrochemical workstation (Autolab 302 N) in the frequency range of 0.01 to 10^5 Hz with an *ac* amplitude of 10 mV.

3. RESULTS AND DISCUSSION

3.1. Structure and Morphology of SiO_x/C@Graphite Composite. Figures 1 and S1 show the SEM images of

https://doi.org/10.1021/acsomega.2c01015
ACS Omega 2022, 7, 15123−15131

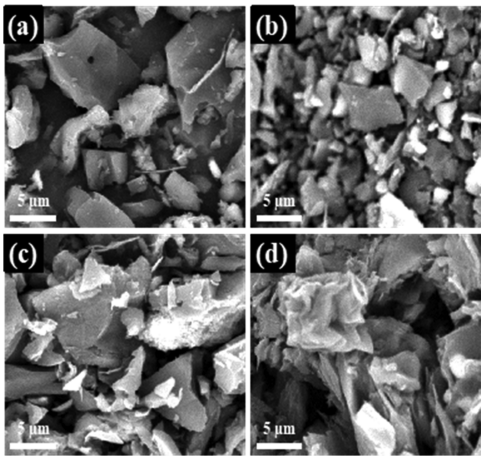

Figure 1. (a–d) SEM images of precursor, SCG-0.5, SCG-1, and SCG-2 samples, respectively.

different samples. As shown in Figure S1a, it can be seen that the surface of original oat husks is regular and flat, which is due to the uniform arrangement of cells on the surface of oat husks. The EDS spectra of the original oat husks are also explored in Figures S2 and S3. As shown in Figures S2 and S3, the oat husk consists of C, O, and Si elements. The distribution of carbon and oxygen is uniform, but silicon is uneven. This phenomenon could be attributed to the structure of the oat husk. Amorphous silica mainly exists on the surface of vascular bundles of oat husks to protect the structure, while organic carbon exists in the whole oat husk framework in the form of lignin and cellulose. The SEM image of precursor is shown in Figure 1a; after carbonization pretreatment, the original regular and flat structure of oat shell is destroyed, part of carbon in oat shell is removed, and SiO_2 is exposed. The high magnification SEM image of the precursor is shown in Figure S4. It can be seen that these SiO_2 particle sizes are nanoscale. The smaller particle size is conducive to alleviate the volume expansion effect of silicon material. The SEM images of three kinds of samples (SCG-0.5, SCG-1, and SCG-2) with different proportions of graphite are exhibited in Figure 1b–d. On the whole, all SCG composites present a block structure with irregular sizes and morphologies, and the particle surfaces are rough, which is consistent with the morphology of millet husk silicon-based composite reported by predecessors.[48] The particle size of the samples became larger with the increase of the graphite, which is mainly due to the bulky morphology of the graphite commodity. However, comparing the SEM (Figure S1b) of commercial graphite with Figure 1b–d, it can be found that graphite and precursor materials are uniformly mixed together after ball milling, which is no longer a larger morphology.

Figure 2a shows the XRD spectrum of the 450 °C precursor. There is a broad peak at 22° which is ascribed to amorphous SiO_2 and carbon. Another broad peak at 42° is the typical peak position on amorphous carbon. Figure 2b shows the XRD patterns of SCG-0.5, SCG-1, and SCG-2, respectively. On the whole, the peak shapes of the three SCG composites are basically similar, indicating that the structure of the SCG composites is not affected by different contents of graphite. Compared with the XRD spectra of the precursor, it can be found that the SCG samples calcined at high temperature have sharp characteristic peaks, showing a good crystal structure. The peaks at 44.3, 44.5, and 54.6° correspond to the (220), (202), and (312) planes of Si (JCPDS NO. 89-9056), respectively, confirming that part of the silica in oat husk is converted into low valence silicon.[15] Due to the addition of graphite, there are peaks at 26.5, 50.7, 59.9, and 77.5°, which corresponds to the (002), (102), (103), and (110) planes of graphite (JCPDS NO. 89-8487). The broad peak at 22° is the overlap of amorphous SiO_2 and carbon. The TG curve of pre-carbonized oat husks is shown in Figure 2c. It can be seen that the weight loss of the sample composed of two parts. When the temperature is below 100 °C, the mass reduction is due to the loss of water in the sample. The obvious weight loss that occurs in the temperature range of 350–550 °C is due to the pyrolysis of organic carbon in the oat husk. It is worth mentioned that the mass of the sample slowly rises at 200–300 °C, which is probably caused by the combination of silicon in oat shell and oxygen in the air to form SiO_2. Finally, when the temperature is 640 °C, the mass of the sample is no longer reduced and is stable at 23.7 wt %. Thus, the content of silicon oxide in SCG-1 is about 11.85 wt %. The surface area and pore size distribution of N_2 can be determined by adsorption area and pore size. The BET method is generally used to analyze the specific surface area, and the BJH model is usually used for pore size distribution. Figure 2d shows the nitrogen adsorption/desorption curves and pore size distribution of SCG-0.5, SCG-1, and SCG-2. The nitrogen adsorption/desorption isotherms of the three composites are all type IV and typical H4 hysteresis loops, indicating that the composites have slit holes generated by particle accumulation. After calculation, the BET specific surface areas of SCG-0.5, SCG-1, and SCG-2 are 296.82, 206.43, and 109.7 $m^2\ g^{-1}$, respectively. The BET surface area of the SCG composite decreases with the increase of graphite content. In addition, the pore size distribution of the three samples is mainly concentrated in the range of 2.5–15 nm (Figure 2e), indicating that the SCG-0.5, SCG-1, and SCG-2 are all mesoporous materials, which is conducive to better electrochemical performance. Figure 2f shows the Raman spectra of the SCG-0.5, SCG-1, and SCG-2 samples. The two separated characteristic peaks at ∼1340 and ∼1580 cm^{-1} correspond to typical D-band and G-band, respectively.[49] D-band corresponds to disordered carbon layer structure and defects, and G-band corresponds to the graphite structure in carbon materials, which is caused by the vibration of the sp^2 hybrid bond of carbon atoms in hexagonal lattice.[49] The I_D/I_G ratio of the SCG-1 composite is 0.66, which indicates that the carbon type of SCG-1 is mainly disordered carbon with more defects. These defects make the conduction of electrons more convenient and improve the circulation efficiency of the electrode. The I_D/I_G strengths of SCG-0.5 and SCG-2 composites are 0.23 and 0.17 respectively, indicating that the carbon in SCG-0.5 and SCG-2 composites is mainly ordered carbon, which is not conducive to electron conduction.

The elemental analyses of SCG-0.5, SCG-1 and SCG-2 by XPS confirmed the existence of silicon, carbon, and oxygen in the samples (Figure 3a). The carbon came from carbonized oat husk and graphite. Figure 3b–d show the high-resolution spectra of the Si (2p) region of SCG-0.5, SCG-1, and SCG-2, respectively. It can be seen that the four characteristic peaks of silicon are located at 103.5, 104.1, 104.5, and 104.5 and 105.2 eV, corresponding to Si^+, Si^{2+}, Si^{3+}, and Si^{4+}, respectively.[1] After calculation, the analytical results of Si^+, Si^{2+}, Si^{3+}, and Si^{4+} ratios in the three samples are shown in Table 1. It is obvious that the content of Si^+ in the SCG-0.5 sample is the highest,

https://doi.org/10.1021/acsomega.2c01015
ACS Omega 2022, 7, 15123–15131

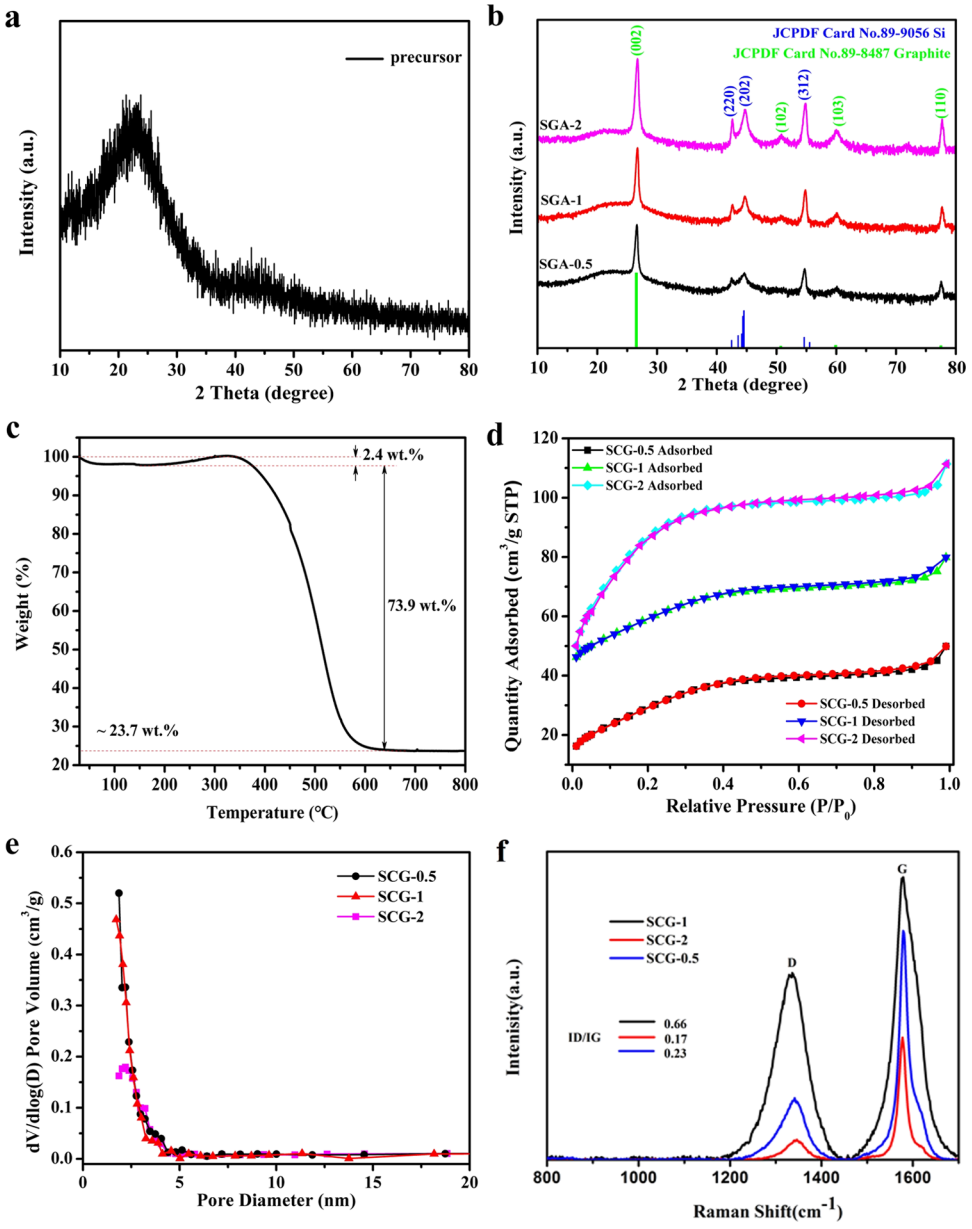

Figure 2. (a) XRD pattern of the precursor; (b) XRD patterns of SCG-0.5, SCG-1, and SCG-2; (c) TG curve of pre-carbonization at 1100 °C oat husk in air atmosphere; (d) nitrogen adsorption/desorption curve of the SCG-0.5, SCG-1, and SCG-2; (e) pore size distribution diagram; and (f) Raman patterns of SCG-0.5, SCG-1, and SCG-2.

followed by SCG-1 and SCG-2. This is because the content of graphite in the SCG-0.5 sample is less, that is, the content of SiO_x is relatively large. The C 1s spectrum of SGA-1 as a typical sample was tested and fitted. As shown in Figure S5, the C 1s spectral region has three peaks at 284.6, 285.8, and 287.9 eV, corresponding to the C═C/C−C, C−O, and C═O bonds, respectively.[45]

3.2. Electrochemical Performances. The electrochemical properties of the SCG-0.5, SCG-1, and SCG-2 were evaluated by assembling into a half-cell with lithium foil as the counter electrode. Figure 4a shows the first three CV curves of the SCG-1 composite at a scan rate of 0.1 mV s^{-1} with a voltage window of 0.01−3.0 V vs Li/Li^+. In the first cycle, there is an obvious broad reduction peak at about 0.7 V, which is related to the formation of solid electrolyte interface (SEI) film, resulting in a low initial coulombic efficiency. Fortunately, this peak disappears in the subsequent cycles. The reduction peak at 0.14 V can be attributed to the alloying of Li_xSi, while the oxidation peak at 0.16 V is mainly attributed to the dealloying of Li_xSi.[30,46] These peaks overlap in the subsequent cycles, which indicates that the SCG-1 composite has good reversibility in the insertion/deinsertion of Li^+.[20] The oxidation peak of graphite at 0.24 V corresponds to the deblocking process of Li_xC composites. For comparison, the CV curves of SCG-0.5 and SCG-2 were also conducted. As shown in Figure S6, it can be clearly seen that the CV curves of the three SCG composites have good consistency, indicating that this kind of electrode materials has high repeatability, which is conducive to the commercial development of the SCG. The charge/discharge voltage curves of SCG-1 in the 1st, 2nd, 20th, 50th, 100th, and 200th cycles at 0.5 A g^{-1} are shown in Figure 4b. The first discharge/charge specific capacity is 1348.6/541.6 mAh g^{-1} with an initial coulombic efficiency of 40.16%. It can be seen that there is a larger capacity loss in this

https://doi.org/10.1021/acsomega.2c01015
ACS Omega 2022, 7, 15123−15131

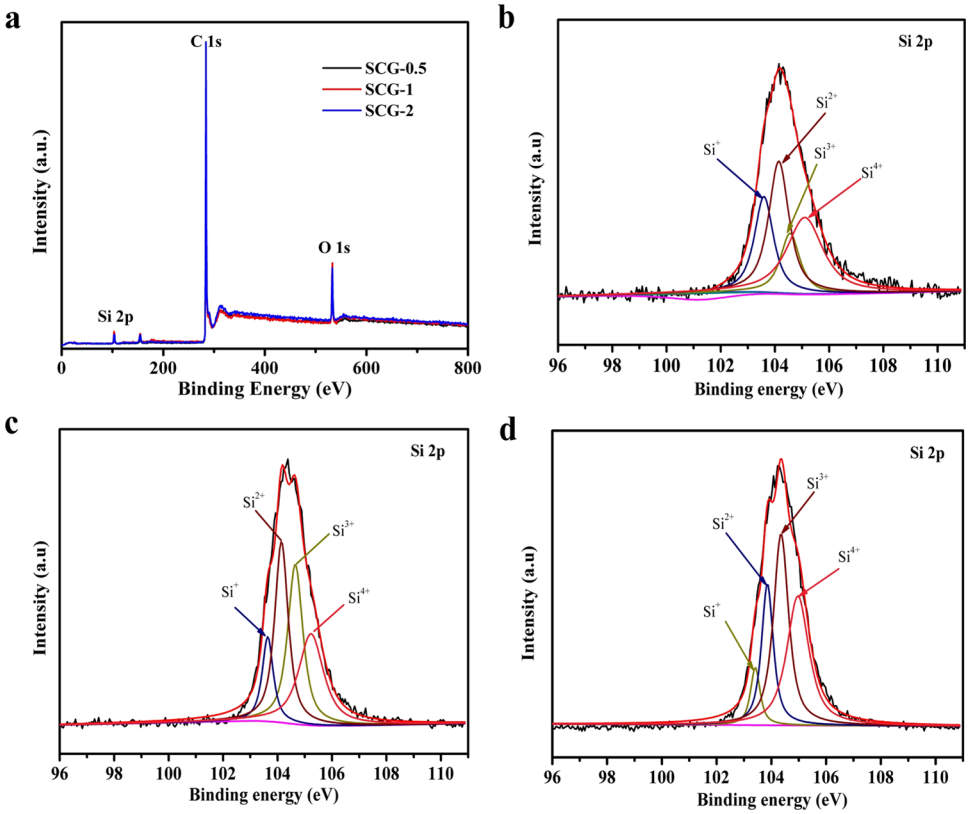

Figure 3. (a) Total XPS spectra of the SCG-0.5, SCG-1, and SCG-2; (b) high-resolution spectra of the Si (2p) regions for SCG-0.5; (c) high-resolution spectra of the Si (2p) regions for SCG-1; and (d) high-resolution spectra of the Si (2p) regions for SCG-2.

Table 1. Proportion of Different Valence Silicon in SCG-0.5, SCG-1, and SCG-2 (Unit: %)

	SCG-0.5	SCG-1	SCG-2
Si^{+}	21.67	11.57	6.95
Si^{2+}	31.82	30.18	20.84
Si^{3+}	13.73	29.97	36.22
Si^{4+}	32.78	28.29	35.99

process, which is consistent with the results of the first cycle of CV. The larger capacity loss is attributed to the inevitable consumption of Li^{+} in the formation of the SEI membrane, electrolyte decomposition, and the formation of Li_2O and Li_4SiO_4 in the first cycle.[50−52] The low initial coulombic efficiency could be effectively improved by the pre-lithium method.[31] In subsequent cycles, the capacity decays continuously due to the repeated volume variations of the silicon, resulting in the continuous formation of new SEI films. At the 20th cycle, the electrode gradually adapted to the volume variations of silicon, and the capacity was the lowest at this time. With the increase of cycles, the continuous infiltration of the electrolyte and more exposed active sites lead to the continuous increase of capacity.

In order to explore the influence of graphite content on the electrochemical performance, we studied the cycle stabilities of SCG-0.5, SCG-1, and SCG-2 as anodes at 0.5 A g^{-1} (Figure 4c). After 200 charge/discharge cycles, the specific capacities of SCG-0.5, SCG-1, and SCG-2 are 468, 601, and 524 mAh g^{-1}, respectively. It is very interesting that the specific capacity of SCG-0.5 is higher than that of the other two materials in the first 10 cycles, but the specific capacity of the SCG-0.5 sample decreases rapidly in the subsequent cycles. It may be because the SCG-0.5 material contains more low valence Si and less graphite, which could deliver higher specific capacity in the initial charge/discharge cycle, but with the increase of cycles, the silicon material will have a larger volume expansion, resulting in crushing and capacity attenuation of the electrode material. On the contrary, the SCG-1 and SCG-2 materials can effectively alleviate the volume variations of Si during cycling because of the more content of graphite than SCG-0.5. In addition, the electrochemical performance of SCG-1 is better than that of SCG-2. Although the conductivity of the SCG-2 composite increased, the specific capacity of SCG-2 decreased to a certain extent because of the low capacity of graphite. In short, the SCG-1 composite exhibits the best cycling performance. These results also indicate that the appropriate amount of graphite plays an important role in the capacity retention of the SCG composite. It should be noted that the reversible specific capacity of SCG-1 first decreases in the first 20 cycles and then gradually increases with the charging/discharging cycles. After 250 cycles, the reversible specific capacity of 809.5 mAh g^{-1} can also be achieved (Figure S7).

Figure 4d shows the rate performances of SCG-0.5, SCG-1, and SCG-2 electrodes. It could be found that the SCG-1 has better lithium storage performance and capacity retention at the current density of 0.1, 0.2, 0.5, 1, 2, and 0.1 A g^{-1}, respectively. The average charge/discharge capacities of SCG-1 were 728.93/788.71, 593.16/615.6, 463.71/473.77, 414.16/425.73, 399.57/401.54, and 648.48/668.67 mAh g^{-1} at the current densities of 0.1, 0.2, 0.5, 1, 2, and 0.1 A g^{-1}, respectively. With the increase of current density, the specific capacities of the three samples all decreased. Even at a high current density of 2 A g^{-1}, the SCG-1 can still provide a specific capacity of 401.54 mAh g^{-1}, which is much higher than

https://doi.org/10.1021/acsomega.2c01015
ACS Omega 2022, 7, 15123−15131

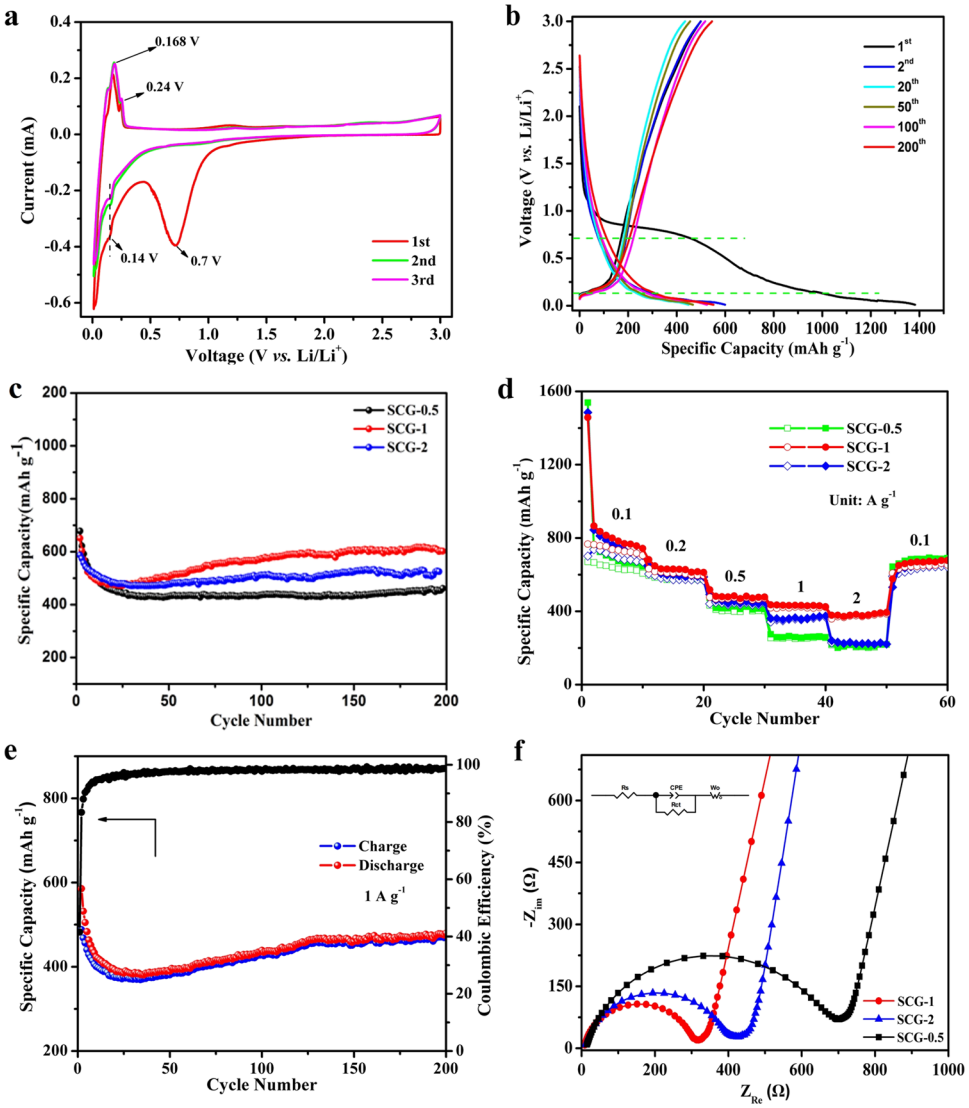

Figure 4. (a) CV curves of SCG-1; (b) charge−discharge curves of the SCG-1 electrode for the 1st, 2nd, 20th, 50th, 100th, and 200th cycles at 0.5 A g^{-1}; (c) cycle performances of SCG-0.5, SCG-1, and SCG-2 at 0.5 A g^{-1}; (d) rate performances of SCG-0.5, SCG-1, and SCG-2; (e) cycle performance of SCG-1 at a high rate of 1 A g^{-1}; and (f) Nyquist plots of SCG-0.5, SCG-1, and SCG-2 electrodes and equivalent circuit diagram before cycling.

the SCG-0.5, SCG-2, and the theoretic capacity of graphite. When the rate returns to 0.1 A g^{-1}, the SCG-1 still delivered a specific capacity of 743.6 mAh g^{-1}, indicating its excellent rate capability. Figure 4e shows the cycling performance of the SCG-1 electrode at a high rate of 1 A g^{-1}. It is interesting that the cycle curves present a "spoon" shape. The specific capacity of the spoon's mouth (at the 2nd cycle) was 591.2 mAh g^{-1}, while the specific capacity of the spoon's bottom was attenuated to 374.5 mAh g^{-1} (at 100th cycle). The specific capacity of the end of the spoon maintained at 455.3 mAh g^{-1} or so (from 125th cycle to 200th cycle). At the 200th cycle, the specific capacity of SCG-1 is still 479.7 mAh g^{-1} with the coulombic efficiency of 98.7%, exhibiting good cycle stability at a high rate of 1 A g^{-1}. The first attenuation is due to the volume expansion effect of silicon particles. The repeated volume changes might break the SEI layer and lead to more extensive exposure of Si active sites in the lithium process. Fresh active sites can provide more charge storage sites, thus resulting in the increase of capacity.[51] The subsequent increase of capacity is attributed to high rate lithium-induced reactivation, which can effectively reorganize the porous microstructure and optimize the stable SEI.[52,53] After the formation and refinement of the stable SEI, the reactivated anode material can show high capacity and excellent cycling performance even at high current density even for a long time.[54]

To explore the electrochemical behaviors, EIS measurements were performed on three SCG hybrids before cycling (Figure 4f). The Nyquist diagram consists of semicircles in the medium and high frequency regions and straight lines in the low frequency regions. The high frequency region corresponds to the charge transfer resistance (R_{ct}) in the equivalent circuit diagram (Inset of Figure 4f). The resistance in the low frequency region is related to the lithium-ion diffusion.[55,56] The fitted data are shown in Table S1. It can be clearly seen that the electrolyte resistance (R_e) difference of the three electrodes is small, while the R_{ct} of SCG-1 (R_{ct} = 283.7 Ω) is much smaller than that of SCG-0.5 (R_{ct} = 659.2 Ω) and SCG-2 (R_{ct} = 409.7 Ω). Thus, it can be inferred that the addition appropriate amount of graphite can effectively improve the

https://doi.org/10.1021/acsomega.2c01015
ACS Omega 2022, 7, 15123−15131

charge transfer rate during charging and discharging, which is conducive to the storage and release of Li^+. In order to further study the excellent electrochemical performance of SCG-1, the Nyquist curve and equivalent circuit diagram before and after cycling are shown in Figure S8. The initial EIS test is carried out on the initial battery before cycling, which is represented by a black line. The frequency semicircle in the EIS profile represents the charge transfer resistance, while the low-frequency line corresponds to the Warburg impedance under ion diffusion control.[51] The equivalent circuit diagram is shown in the lower right corner of Figure S8. After 50 cycles, the EIS test was conducted again, which is indicated by a red line (Figure S8). It is not difficult to see that there is a semicircle in the high frequency region and the intermediate frequency region, which is due to the formation of an SEI after cycling.[55] The first semicircle in the high frequency region is represented by R_e in the equivalent circuit, while the second semicircle in the intermediate frequency region is represented by R_{ct}. The equivalent circuit model was composed of R_e, SEI resistance (R_s), R_{ct}, Warburg impedance (W_1), and constant phase element. The fitted impedance parameters are listed in Table 2. As can be seen from Table 2, the R_e shows a small value before and after 50th cycle. The R_{ct} of SCG-1 at 50th (79.6 Ω) is much smaller than the initial value of 283.7 Ω, indicating that the SEI is gradually formed and continuously optimized after cycling. At 50th discharge/charge cycle, the lithiation-induced reactivation and optimization of SEI make charge transfer easier, resulting in the reduction of R_{ct} and the increase of capacity, which is consistent with the previous results of Figure 4e. This result further confirmed that SCG-1 has excellent structural stability and good electrochemical performance.

Table 2. Electrochemical Impedance Parameters of the SCG-1 Electrode before and after the 50th Cycle

samples	R_e (Ω)	R_s (Ω)	R_{ct} (Ω)
before	3.19		283.7
50th	2.05	74.1	79.6

4. CONCLUSIONS

In conclusion, a low-cost and high-capacity SiO_x/C@graphite (SCG) hybrid derived from oat husks were prepared by a simple argon/hydrogen reduction method. At the same time, the influence of the content of graphite on the electrochemical properties of SCG composites was also investigated. As an advanced anode for LIBs, the SCG-1 composite exhibits an excellent electrochemical performance in terms of lithium storage capacity (809.5 mAh g^{-1} at 0.5 A g^{-1} even after 250th cycles) and high rate capability (479.7 mAh g^{-1} at 1 A g^{-1} after 200th cycle). This kind of SCG electrode materials shows high repeatability, which is conducive to the commercial development. This work may be pave the way for developing a low-cost silicon-based anode derived from biomass with a large reversible capacity and long cycle life in LIBs.

ASSOCIATED CONTENT

Supporting Information

The Supporting Information is available free of charge at https://pubs.acs.org/doi/10.1021/acsomega.2c01015.

Characterization of materials, SEM, EDS, XPS, and electrochemical properties (PDF)

AUTHOR INFORMATION

Corresponding Author

Hongxun Yang − *School of Environmental & Chemical Engineering, Jiangsu University of Science and Technology, Zhenjiang, Jiangsu 212003, China; Yunfan (Zhenjiang) New Energy Materials, Co. Ltd., Zhenjiang, Jiangsu 212050, China;* orcid.org/0000-0003-1445-3468; Email: yhongxun@126.com

Authors

Mengfei Sun − *School of Environmental & Chemical Engineering, Jiangsu University of Science and Technology, Zhenjiang, Jiangsu 212003, China*

Jiaojiao Ma − *School of Environmental & Chemical Engineering, Jiangsu University of Science and Technology, Zhenjiang, Jiangsu 212003, China*

Minghang Xu − *School of Environmental & Chemical Engineering, Jiangsu University of Science and Technology, Zhenjiang, Jiangsu 212003, China*

Jianzi Zhang − *Jiangsu Runchao Energy Storage Technology Co., Ltd., Zhenjiang, Jiangsu 212050, China*

Changhua Wang − *ZhenjiangDongya Carbon Coke, Co. Ltd., Zhenjiang, Jiangsu 212003, China*

Complete contact information is available at: https://pubs.acs.org/10.1021/acsomega.2c01015

Author Contributions

The manuscript was written through contributions of all authors. All authors have given approval to the final version of the manuscript.

Notes

The authors declare no competing financial interest.

ACKNOWLEDGMENTS

This work was financially supported by the Foundation from Primary Research & Development Plan of Zhenjiang (GY2021019), Natural Science Foundation of Jiangsu Province for Youths (BK20170571), and the Modern Agricultural Projects of Zhenjiang (NY2019022).

REFERENCES

(1) Li, F.; Deng, C. H.; Liu, X.; Ding, Y. H.; Peng, J. F. SiO_x-Modified Biocarbon Materials Derived from Shaddock Peel for Li-Ion Batteries. *ChemistrySelect* **2019**, *4*, 8614−8620.

(2) Wu, B.; Xie, Y.; Meng, Y. Q.; Qian, C.; Chen, Y. Y.; Yuan, A. H.; Guo, X. M.; Yang, H. X.; Wan, S. J.; Lin, S. L. Construction of unique heterogeneous cobalt-manganese oxide porous microspheres for the assembly of long-cycle and high-rate lithium ion battery anodes. *J. Mater. Chem. A* **2019**, *7*, 6149−6160.

(3) Wang, Z.; Zhang, Z.; Xia, J.; Wang, W.; Sun, S.; Liu, L.; Yang, H. Fe_2O_3@C core@shell nanotubes: Porous Fe_2O_3 nanotubes derived from MIL-88A as cores and carbon as shells for high power lithium ion batteries. *J. Alloys Compd.* **2018**, *769*, 969−976.

(4) Yang, H.; Song, T.; Liu, L.; Devadoss, A.; Xia, F.; Han, H.; Park, H.; Sigmund, W.; Kwon, K.; Paik, U. Polyaniline/Polyoxometalate Hybrid Nanofibers as Cathode for Lithium Ion Batteries with Improved lithium storage capacity. *J. Phys. Chem. C* **2013**, *117*, 17376−17381.

(5) Chu, H. Y.; Wu, Q. Z.; Huang, J. G. Rice husk derived silicon/carbon and silica/carbon nanocomposites as anodic materials for lithium-ion batteries. *Colloids Surf. A Physicochem. Eng. Asp.* **2018**, *558*, 495−503.

(6) Wong, D. P.; Suriyaprabha, R.; Yuvakumar, R.; Rajendran, V.; Chen, Y. T.; Hwang, B. J.; Chen, L. C.; Chen, K. H. Binder-free rice

husk-based silicon-graphene composite as energy efficient Li-ion battery anodes. *J. Mater. Chem. A* **2014**, *2*, 13437−13441.
(7) Sun, M.; Sun, M.; Yang, H.; Song, W.; Nie, Y.; Sun, S. Porous Fe_2O_3 nanotubes as advanced anode for high performance lithium ion batteries. *Ceram. Int.* **2017**, *43*, 363−367.
(8) Sun, M. F.; Chu, X. F.; Wang, Z. K.; Yang, H. X.; Yang, Z.; Ma, J. J.; Zhou, B.; Yang, T. Y.; Chen, L. Z. Rosa roxburghii-like hierarchical hollow sandwich-structure C@Fe_2O_3@C microspheres as second nanomaterialsfor superior lithium storage. *J. Alloys Compd.* **2021**, *855*, No. 157518.
(9) Wang, Y.; Guo, X. M.; Wang, Z. K.; Lü, M.; Wu, B.; Wang, Y.; Yan, C.; Yuan, A. H.; Yang, H. X. Controlled pyrolysis of MIL-88A to Fe_2O_3@C nanocomposites with varied morphologies and phases for advanced lithium storage. *J. Mater. Chem. A* **2017**, *5*, 25562−25573.
(10) Guo, S. P.; Ma, Z.; Li, J. C.; Xue, H. G. Facile preparation and promising lithium storage ability of alpha-$LiFeO_2$/porous carbon nanocomposite. *J. Alloys Compd.* **2017**, *711*, 8−14.
(11) Guo, S. P.; Ma, Z.; Li, J. C.; Xue, H. G. First investigation of the electrochemical performance of gamma-$LiFeO_2$ micro-cubes as promising anode material for lithium-ion batteries. *J. Mater. Sci.* **2017**, *52*, 1469−1476.
(12) Li, J. C.; Feng, F.; Yang, S. H.; Gu, Y. R.; Xue, H. G.; Guo, S. P. Promising electrochemical performance of $Cu_3Mo_2O_9$ nanorods for lithium-ion batteries. *J. Mater. Sci.* **2017**, *52*, 12380−12389.
(13) Yang, S. H.; Xue, H. G.; Guo, S. P. Borates as promising electrode materials for rechargeable batteries. *Coord. Chem. Rev.* **2021**, *427*, No. 213551.
(14) Liu, N.; Huo, K. F.; McDowell, M. T.; Zhao, J.; Cui, Y. Rice husks as a sustainable source of nanostructured silicon for high performance Li-ion battery anodes. *Sci. Rep.* **2013**, *3*, 1919.
(15) Wang, L. P.; Xue, J.; Gao, B.; Gao, P.; Mou, C. X.; Li, J. Rice husk derived carbon-silica composites as anodes for lithium ion batteries. *RSC Adv.* **2014**, *4*, 64744−64746.
(16) Ju, Y. M.; Tang, J. A.; Zhu, K.; Meng, Y.; Wang, C. Z.; Chen, G.; Wei, Y. J.; Gao, Y. SiO_x/C composite from rice husks as an anode material for lithium-ion batteries. *Electrochim. Acta* **2016**, *191*, 411−416.
(17) Wang, G. Q.; Wen, Z. S.; Yang, Y. E.; Yin, J. P.; Kong, W. Q.; Li, S.; Sun, J. C.; Ji, S. J. Ultra-long life Si@rGO/g-C_3N_4 with a multiply synergetic effect as an anode material for lithiumion batteries. *J. Mater. Chem. A* **2018**, *6*, 7557−7565.
(18) Wang, Z. F.; Smith, A. T.; Wang, W. X.; Sun, L. Y. Versatile Nanostructures from Rice Husk Biomass for Energy Applications. *Angew. Chem., Int. Ed.* **2018**, *57*, 13722−13734.
(19) Li, Z. Z.; Wang, W.; Li, Z. H.; Qin, Z.; Wang, J.; Liu, Z. Bridging porous Si-C composites with conducting agents for improving battery cycle life. *J. Power Sources* **2015**, *286*, 534−539.
(20) Li, G.; Li, J. Y.; Yue, F. S.; Xu, Q.; Zuo, T. T.; Yin, Y. X.; Guo, Y. G. Reducing the volume deformation of high capacity SiO_x/G/C anode toward industrial application in high energy density lithium-ion batteries. *Nano Energy* **2019**, *60*, 485−492.
(21) Xu, Q.; Sun, J. K.; Yu, Z. L.; Yin, Y. X.; Xin, S.; Yu, S.-H.; Guo, Y. G. SiO_x Encapsulated in Graphene Bubble Film: An Ultrastable Li-Ion Battery Anode. *Adv. Mater.* **2018**, *30*, No. 1707430.
(22) Yang, J. P.; Wang, Y. X.; Li, W.; Wang, L. J.; Fan, Y. C.; Jiang, W.; Luo, W.; Wang, Y.; Kong, B.; Selomulya, C.; Liu, H. K.; Dou, S. X.; Zhao, D. Y. Amorphous TiO_2 Shells: A Vital Elastic Buffering Layer on Silicon Nanoparticles for High-Performance and Safe Lithium Storage. *Adv. Mater.* **2017**, *29*, No. 1700523.
(23) Wu, J. X.; Cao, Y. L.; Zhao, H. M.; Mao, J. F.; Guo, Z. P. The critical role of carbon in marrying silicon and graphite anodes for high-energy lithium-ion batteries. *Carbon Energy* **2019**, *1*, 57−76.
(24) Wu, W.; Wang, M.; Wang, J.; Wang, C. Y.; Deng, Y. H. Green Design of Si/SiO_2/C Composites as High-Performance Anodes for Lithium-Ion Batteries. *ACS Appl. Energy Mater.* **2020**, *3*, 3884−3892.
(25) Rehman, W. U.; Wang, H. F.; Manj, R. Z. A.; Luo, W.; Yang, J. P. When Silicon Materials Meet Natural Sources: Opportunities and Challenges for Low-Cost Lithium Storage. *Small* **2021**, *17*, No. 904508.
(26) Yuan, M. J.; Guo, X. T.; Liu, Y.; Pang, H. Si-based materials derived from biomass: synthesis and applications in electrochemical energy storage. *J. Mater. Chem. A* **2019**, *7*, 22123−22147.
(27) Ma, T. Y.; Xu, H. Y.; Yu, X. N.; Li, H. Y.; Zhang, W. G.; Cheng, X. L.; Zhu, W. T.; Qiu, X. Lithiation Behavior of Coaxial Hollow Nanocables of Carbon-Silicon Composite. *ACS Nano* **2019**, *13*, 2274−2280.
(28) Li, J. Y.; Li, G.; Zhang, J.; Yin, Y. X.; Yue, F. S.; Xu, Q.; Guo, Y. G. Rational Design of Robust Si/C Microspheres for High-Tap-Density Anode Materials. *ACS Appl. Mater. Interfaces* **2019**, *11*, 4057−4064.
(29) Jia, H. P.; Zou, L. F.; Gao, P. Y.; Cao, X.; Zhao, W. G.; He, Y.; Engelhard, M. H.; Burton, S. D.; Wang, H.; Ren, X. D.; Li, Q. Y.; Yi, R.; Zhang, X.; Wang, C. M.; Xu, Z. J.; Li, X. L.; Zhang, J. G.; Xu, W. High-Performance Silicon Anodes Enabled By Nonflammable Localized High-Concentration Electrolytes. *Adv. Energy Mater.* **2019**, *9*, No. 1900784.
(30) Guo, C. F.; Xie, Y.; Pan, K.; Li, L. MOF-derived hollow SiO(x)nanoparticles wrapped in 3D porous nitrogen-doped graphene aerogel and their superior performance as the anode for lithium-ion batteries. *Nanoscale* **2020**, *12*, 13017−13027.
(31) Chen, L. Y.; Zheng, J.; Lin, S. Y.; Khan, S.; Huang, J. L.; Liu, S. H.; Chen, Z. R.; Wu, D. C.; Fu, R. W. Synthesis of SiO_x/C Composite Nanosheets As High-Rate and Stable Anode Materials for Lithium-Ion Batteries. *ACS Appl. Energy Mater.* **2020**, *3*, 3562−3568.
(32) Yan, Z.; Guo, J. C. High-performance silicon-carbon anode material via aerosol spray drying and magnesiothermic reduction. *Nano Energy* **2019**, *63*, 103845.
(33) Huang, S. S.; Tung, M. T.; Huynh, C. D.; Hwang, B. J.; Bieker, P. M.; Fang, C. C.; Wu, N. L. Engineering Rice Husk into a High-Performance Electrode Material through an Ecofriendly Process and Assessing Its Application for Lithium-Ion Sulfur Batteries. *ACS Sustainable Chem. Eng.* **2019**, *7*, 7851−7861.
(34) Fu, R. S.; Li, Y. S.; Wu, Y. K.; Shen, C. X.; Fan, C. Z.; Liu, Z. P. Controlling siloxene oxidization to tailor SiO_x anodes for high performance lithium ion batteries. *J. Power Sources* **2019**, *432*, 65−72.
(35) Fan, X.; Ji, J. J.; Jiang, X. P.; Wang, W.; Liu, Z. P. Facile fabrication of stable and high-rate Si/$NiSi_x$/CNTs Li-ion anodes with a buffering interface. *RSC Adv.* **2016**, *6*, 78559−78563.
(36) Fan, X.; Jiang, X. P.; Wang, W.; Liu, Z. P. Green synthesis of nanoporous Si/C anode using NaCl template with improved cycle life. *Mater. Lett.* **2016**, *180*, 109−113.
(37) Shen, C. X.; Fu, R. S.; Xia, Y. G.; Liu, Z. P. New perspective to understand the effect of electrochemical prelithiation behaviors on silicon monoxide. *RSC Adv.* **2018**, *8*, 14473−14478.
(38) Shen, C. X.; Fu, R. S.; Guo, H. C.; Wu, Y. K.; Fan, C. Z.; Xia, Y. G.; Liu, Z. P. Scalable synthesis of Si nanowires interconnected SiO_x anode for high performance lithium-ion batteries. *J. Alloys Compd.* **2019**, *783*, 128−135.
(39) Zuo, X. X.; Xia, Y. G.; Ji, Q.; Gao, X.; Yin, S. S.; Wang, M. M.; Wang, X. Y.; Qiu, B.; Wei, A. X.; Sun, Z. C.; Liu, Z. P.; Zhu, J.; Cheng, Y. J. Self-Templating Construction of 3D Hierarchical Macro−/Mesoporous Silicon from 0D Silica Nanoparticles. *ACS Nano* **2017**, *11*, 889−899.
(40) Liu, Z. H.; Yu, Q.; Zhao, Y. L.; He, R. H.; Xu, M.; Feng, S. H.; Li, S. D.; Zhou, L.; Mai, L. Q. Silicon oxides: a promising family of anode materials for lithium-ion batteries. *Chem. Soc. Rev.* **2019**, *48*, 285−309.
(41) Ren, Y. R.; Li, M. Q. Facile synthesis of SiO_x@C composite nanorods as anodes for lithium ion batteries with excellent electrochemical performance. *J. Power Sources* **2016**, *306*, 459−466.
(42) Chen, T. J.; Zhang, J.; Wang, Z. Q.; Zhao, R. D.; He, J. J.; Wu, J. H.; Qin, J. G. Oxygen-enriched gasification of lignocellulosic biomass: Syngas analysis, physicochemical characteristics of the carbon-rich material and its utilization as an anode in lithium ion battery. *Energy* **2020**, *212*, No. 118771.
(43) Zhao, J. K.; Wei, D. N.; Zhang, X. B.; Zhang, S. G.; Zhang, C.; Yang, X. J. Biomass-derived hierarchical N, P codoped porous 3D-

https://doi.org/10.1021/acsomega.2c01015
ACS Omega 2022, 7, 15123−15131

carbon framework@TiO_2 hybrids as advanced anode for lithium ion batteries. *J. Colloid Interface Sci.* **2022**, *606*, 577−587.
(44) Guo, X. T.; Li, W. T.; Geng, P. B.; Zhang, Q. Y.; Pang, H.; Xu, Q. Construction of SiO_x/nitrogen-doped carbon superstructures derived from rice husks for boosted lithium storage. *J. Colloid Interface Sci.* **2022**, *606*, 784−792.
(45) Chen, W. Y.; Xu, D. H.; Kuang, S. J.; Wu, Z. Q.; Hu, H.; Zheng, M. T.; Yu, X. Y. Hierarchically porous SiO_x/C and carbon materials from one biomass waste precursor toward high-performance lithium/sodium storage. *J. Power Sources* **2021**, *489*, No. 229459.
(46) Madani Hosseini, M.; Shao, Y. X.; Whalen, J. K. Biocement production from silicon-rich plant residues: Perspectives and future potential in Canada. *Biosyst. Eng.* **2011**, *110*, 351−362.
(47) Xu, M. H.; Ma, J. J.; Niu, G. L.; Yang, H. X.; Sun, M. F.; Zhao, X. C.; Yang, T. Y.; Chen, L. Z.; Wang, C. H. A Low-Cost and High-Capacity SiO_x/C@graphite Hybrid as an Advanced Anode for High-Power Lithium-Ion Batteries. *ACS Omega* **2020**, *5*, 16440−16447.
(48) Cui, J. L.; Cheng, F. P.; Lin, J.; Yang, J. C.; Jiang, K.; Wen, Z. S.; Sun, J. C. High surface area C/SiO_2 composites from rice husks as a high-performance anode for lithium ion batteries. *Powder Technol.* **2017**, *311*, 1−8.
(49) Zhang, K. X.; Yang, H. X.; Lü, M. F.; Yan, C.; Wu, H.; Yuan, A. H.; Lin, S. L. Porous MoO_2-Cu/C/Graphene nano-octahedrons quadruple nanocomposites as an advanced anode for lithium ion batteries with enhanced rate capability. *J. Alloys Compd.* **2018**, *731*, 646−654.
(50) Kim, J. H.; Park, C. M.; Kim, H. S.; Kim, Y. J.; Sohn, H. J. Electrochemical behavior of SiO anode for Li secondary batteries. *J. Electroanal. Chem.* **2011**, *661*, 245−249.
(51) Jung, S. C.; Kim, H. J.; Kim, J. H.; Han, Y. K. Atomic-Level Understanding toward a High-Capacity and High Power Silicon Oxide (SiO) Material. *J. Phys. Chem. C* **2016**, *120*, 886−892.
(52) Yang, H. X.; Li, L. Tin-indium/Graphene with Enhanced Initial Coulombic Efficiency and Rate Performance for Lithium Ion Batteries. *J. Alloys Compd.* **2014**, *584*, 76−80.
(53) Xia, Q.; Xu, A. D.; Huang, C. Y.; Yan, Y. R.; Wu, S. P. Porous Si@SiO_x@N-Rich Carbon Nanofibers as Anode in Lithium-Ion Batteries under High Temperature. *ChemElectroChem* **2019**, *6*, 4402−4410.
(54) Zhao, X. C.; Niu, G. L.; Yang, H. X.; Ma, J. J.; Sun, M. F.; Xu, M. H.; Xiong, W. W.; Yang, T. Y.; Chen, L. Z.; Wang, C. H. MIL-88A@polyoxometalate microrods as an advanced anode for high-performance lithium ion batteries. *CrystEngComm* **2020**, *22*, 3588−3597.
(55) Yang, H. X.; Xie, Y.; Zhu, M. M.; Liu, Y. M.; Wang, Z. K.; Xu, M. H.; Lin, S. L. Hierarchical porous $MnCo_2O_4$ yolk-shell microspheres from MOFs as secondary nanomaterials for high power lithium ion batteries. *Dalton Trans.* **2019**, *48*, 9205−9213.
(56) Yang, H. X.; Wu, B.; Liu, Y. M.; Wang, Z. K.; Xu, M. H.; Yang, T. Y.; Chen, Y. Y.; Wang, C. H.; Lin, S. L. Porous Multicomponent Mn-Sn-Co Oxide Microspheres as Anodes for High-Performance Lithium-Ion Batteries. *ACS Omega* **2019**, *4*, 16016−16025.

https://doi.org/10.1021/acsomega.2c01015
ACS Omega 2022, 7, 15123−15131